Achieving High Thermoelectric Performance in Mixed Natural-Synthetic Tetrahedrites

Petr Levinský, Pavan Kumar Ventrapati, Anne Dauscher, Jiří Hejtmánek, Christophe Candolfi, Pr. Bertrand Lenoir

Achieving high thermoelectric performance in mixed natural-synthetic tetrahedrites

Petr Levinský,[*[a,b,c]] Pavan Kumar Ventrapati,[[a]] Anne Dauscher,[[a]] Jiří Hejtmánek,[[b]] Christophe Candolfi,[*[a]] Bertrand Lenoir[*[a]]

[a] Dr. P. Levinský, Dr. P. Kumar Ventrapati, Dr. A. Dauscher, Dr. C. Candolfi, Pr. B. Lenoir

Institut Jean Lamour, UMR 7198 CNRS – Université de Lorraine, Campus ARTEM, 2 allée André Guinier, BP 50840, 54011 Nancy, France

E-mail: bertrand.lenoir@univ-lorraine.fr

[b] Dr. P. Levinský, Dr. J. Hejtmánek

FZU – Institute of Physics of the Czech Academy of Sciences, Cukrovarnická 10/112, 162 00, Prague 6, Czech Republic

E-mail: levinsky@fzu.cz

[c] Dr. P. Levinský

Faculty of Nuclear Sciences and Physical Engineering, Czech Technical University in Prague, Prague, Czech Republic

Abstract: Tetrahedrites, a class of naturally-occurring sulfosalts, recently emerged as interesting thermoelectric materials due to their semiconducting electronic properties combined with glass-like thermal transport. Here, we demonstrate that the high thermoelectric performance of synthetic tetrahedrites can be maintained while being mixed with tetrahedrite minerals. The combination of ball-milling and spark plasma sintering yields chemically-homogeneous, dense polycrystalline samples with thermoelectric performance equivalent to those obtained in purely synthetic compounds with peak *ZT* values of ~0.6 at 623 K. While ball-milling significantly lowers the crystallite size, a complete solid solution between both

types of tetrahedrites is only achieved through the sintering process. Not only do these findings confirm interesting prospects for the direct use of natural ores in the preparation of tetrahedrites, but they also further evidence the importance of the chemical compositions of the two initial tetrahedrites on the optimization of the thermoelectric properties of the final compound.

Introduction

Thermoelectric devices enable solid-state conversion of heat into electricity and vice versa, offering interesting prospects to convert waste heat into useful electrical energy.[1,2] However, a good thermoelectric material should strike a delicate balance between a large Seebeck coefficient α, a low electrical resistivity ρ and a low total thermal conductivity κ. Optimizing these three transport coefficients, interdependent via the carrier concentration, is pivotal to maximizing the dimensionless thermoelectric figure of merit $ZT = \alpha^2 T/\rho\kappa$ at an operating absolute temperature T.[1,2] In addition to these prerequisites, often met in heavily-doped semiconductors with complex crystal structures,[1-4] the cost, toxicity and scarcity of the elements entering the chemical composition of thermoelectric materials can severely limit their widespread use in thermoelectric generators. Possible strategies to overcome this problem include the design of new materials consisting of earth-abundant and environmentally-friendly elements or the direct use of mineral ores without adjustment of their chemical compositions. Fulfilling these requirements, sulfides have drawn attention over the last few years with several families exhibiting high thermoelectric performance with ZT values reaching unity typically around 700 K. $Cu_{2-x}S$,[5,6] bornite Cu_5FeS_4,[7,8] chalcopyrite $CuFeS_2$,[9-11] kesterite-like Cu_2TMS_4 (T = Fe, Co, Ni, Zn; M = Ge, Sn),[12-14] colusites $Cu_{26}T_2M_6S_{32}$ (T = Nb, Ta, Cr, Mo, Ti, V, W; M = Ge, Sn, Sb) [15-18] and Cu_2SnS_3 [19-25] are few examples of such systems.

Tetrahedrites are a class of minerals of general chemical formula $Cu_{12-x}M_x(Sb,As)_4S_{13}$ (*M* = transition metals such as Mn, Fe, Co, Ni or Zn or metalloids such as Sn, Ge or Pb; $0 \leq x \leq 2$), naturally occurring all over the world, that also conform to the above-mentioned strategies. Thanks to their versatile chemistry and inherent very low thermal conductivity similar to amorphous compounds, tetrahedrites have recently emerged as a family of prospective materials for thermoelectric applications in power generation near 700 K.[26-54] Being intrinsically *p*-type regardless of the chemical composition, the hole concentration can be easily tuned through varying the nature and the concentration of the *M* element substituting on the Cu sites. This partial substitution enables to drive the metallic tetrahedrite $Cu_{12}Sb_4S_{13}$ towards a heavily-doped semiconducting state before eventually entering a semiconducting regime when two electrons per formula unit are added which, for most of the *M* elements considered so far, corresponds to $x = 2$ in the above-mentioned chemical formula. In optimally-doped tetrahedrites, this favorable combination of electronic and thermal properties leads to *ZT* values ranging between 0.7 and 1.0 near 700 K.[26-55]

While various attempts at shortening the processing time required to prepare optimized tetrahedrites have been considered via ball-milling or melt-spinning,[51,53] these interesting alternatives to conventional powder metallurgy routes still require long processing or annealing times. The direct use of natural tetrahedrite ores, which are still nowadays mined in various locations, may offer an interesting solution to overcome these drawbacks. Preliminary results have shown that mixing minerals with synthetic compounds can produce polycrystalline samples with *ZT* values close to unity near 700 K.[28] These results, obtained by mixing the ternary tetrahedrite $Cu_{12}Sb_4S_{13}$ with minerals originating from Peru, have indicated that a combination of ball-milling and spark plasma sintering yields a homogeneous final compound despite the very different chemical compositions of the raw materials.[28] However, the formation mechanism of homogeneous samples as well as the influence of the chemical

compositions of the mineral and synthetic tetrahedrite on the thermoelectric properties of the final compound are yet to be fully elucidated.

Here, we explore these issues and extend prior results with a detailed investigation of the phase formation and thermoelectric properties (5 – 700 K) of mixed natural-synthetic tetrahedrites. The tetrahedrite minerals considered in this study, that originate from three different geographical locations (France, Peru and Mexico), were chosen to determine the influence of the initial chemical composition on the thermoelectric properties of the final compound. These natural ores were mixed with either the ternary $Cu_{12}Sb_4S_{13}$ or Ni-substituted $Cu_{11}NiSb_4S_{13}$ tetrahedrite, both of which exhibit metallic-like transport properties,[26,27,29] used in an effort to counterbalance the semiconducting properties of the minerals. Our results demonstrate that the chemical composition of the mineral and synthetic tetrahedrite as well as the synthetic-to-mineral ratio are the key parameters to optimize the thermoelectric properties of the final composite. While short-term ball-milling provides an efficient way for mixing the powders of the two compounds and reducing the grain size, the consolidation of the mixture of highly-reactive powders under high-temperature conditions by spark plasma sintering is the main step that leads to the formation of a chemically-homogeneous, dense bulk pellet. Most importantly, we show that using up to 50% of natural ore results in a peak *ZT* value equivalent to that of the synthetic tetrahedrite. These results open interesting prospects as to the direct use of mineral ores in the synthesis of tetrahedrites with optimized thermoelectric properties.

Results and Discussion

Synthesis and chemical composition

In this study, three tetrahedrites ores, the composition of which are listed in Table 1, were considered for the synthesis of synthetic-mineral composites. Each of them shows a distinct As-

to-Sb ratio, with the mineral from France and Mexico corresponding to a nearly pure tetrahedrite (Sb-rich) and tennantite (As-rich), respectively, and the sample originating from Peru corresponding to a solid solution of both minerals. The difference in the As-to-Sb ratio is the main chemical quantity that determines the lattice parameter of the cubic unit cell.[41]

Table 1. Lattice parameters inferred from Rietveld refinements against the PXRD data and actual chemical compositions of the samples measured by EPMA for the minerals. All the chemical compositions are normalized to 29 atoms per formula unit.

Origin	*EPMA composition*	*a (Å)*
Peru	$Cu_{10.03}Ag_{0.03}Zn_{1.78}Fe_{0.14}Sb_{1.28}As_{2.75}S_{12.99}$	10.288(1)
Mexico	$Cu_{9.93}Ag_{0.01}Zn_{1.56}Fe_{0.37}Sb_{0.46}As_{3.66}S_{12.97}$	10.220(1)
France	$Cu_{10.21}Ag_{0.02}Zn_{1.15}Fe_{0.71}Sb_{3.82}As_{0.02}S_{13.06}$	10.378(2)

To monitor the evolution of the mixed powders throughout the ball-milling process, a small amount of powders was sampled at regular time intervals and studied by powder X-ray diffraction and scanning electron microscopy. As an example, Figure 1a and 1b shows the PXRD patterns of the mixture of synthetic $Cu_{12}Sb_4S_{13}$ and Peru mineral, and of synthetic $Cu_{11}NiSb_4S_{13}$ and France mineral, respectively. Similar evolutions of the PXRD patterns occur for the Ni-substituted tetrahedrite mixed with these minerals.

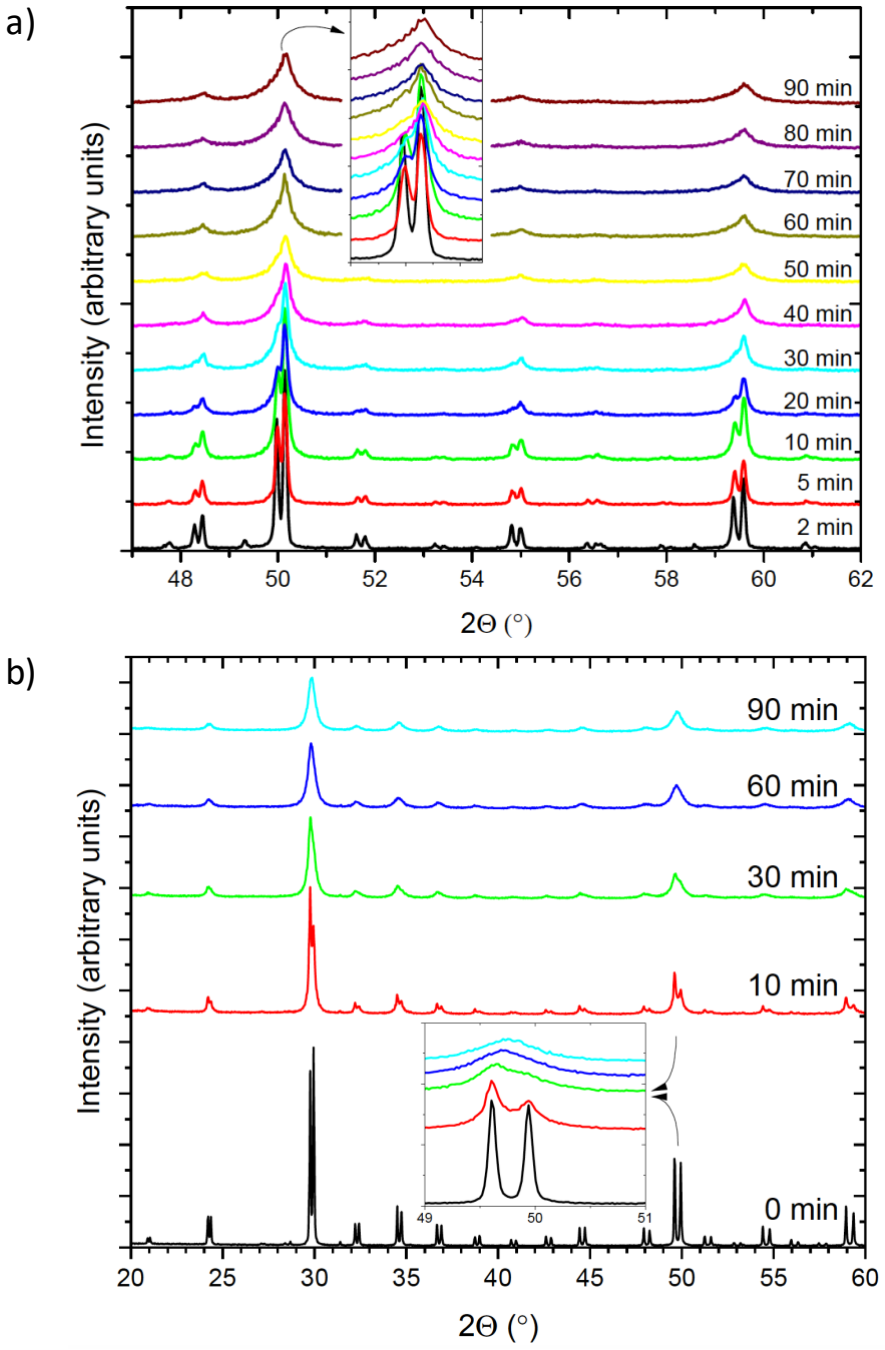

Figure 1. Evolution of the powder X-ray diffraction pattern of the 50:50 mixture of a) synthetic $Cu_{12}Sb_4S_{13}$ and Peru tetrahedrites and b) synthetic $Cu_{11}NiSb_4S_{13}$ and France tetrahedrites as a function of the ball-milling time.

For the $Cu_{12}Sb_4S_{13}$ – Peru mixture, the PXRD pattern collected after only 2 min of ball-milling exhibits two well-defined series of reflections that correspond to the synthetic and natural

tetrahedrites, the lattice parameter of which significantly differs due to their distinct chemical compositions (a = 10.320 and 10.288 Å for the synthetic and natural tetrahedrites, respectively). As the ball-milling process progresses further, the diffraction peaks significantly broaden due to the decrease in the crystallite size from the micro to the nanoscale. Meanwhile, the peak intensity is strongly reduced for the same reason. Regardless of the ball-milling time, however, the positions of the two series of peaks remain unchanged. The seemingly merging of the main peaks into broad, single peaks reflects their strong broadening rather than marking an evolution of the peak position governed by the chemical composition. Thus, the unchanged angular position of the two series of reflections suggests that the two-phase nature of the powders is maintained throughout the ball-milling process, without any evident reaction between the two phases. In addition, even after 90 min of ball-milling, no formation of secondary phases is evidenced by PXRD. A similar evolution is observed for the $Cu_{11}NiSb_4S_{13}$ – France mixture (Figure 1b). These results further show that the intensity of the peaks associated with the synthetic phase decays faster than that of the peaks of the mineral. This is likely a direct consequence of the softer nature of the synthetic phase compared to the mineral resulting in a faster decrease in the particle size. The difference in the mechanical properties between the two samples is supported by ultrasonic measurements of the elastic moduli of the synthetic $Cu_{12}Sb_4S_{13}$ and of various minerals indicating that the latter exhibit higher Young's modulus, shear modulus and hardness by up to 40%.[28,57]

These conclusions are corroborated by SEM experiments, which clearly show the presence of the two $Cu_{12}Sb_4S_{13}$ and Peru phases (Figure 2). This further confirms that they do not chemically interact during the ball-milling process and that their chemical composition is preserved up to 30 min of ball-milling. For ball-milling time of 60 min, the two phases can no longer be resolved by SEM, suggesting that the size of the particles has crossed the detection limit of this technique. Energy dispersive X-ray spectroscopy (EDXS) mappings performed on

mixed powders (Figure 3) of $Cu_{11}NiSb_4S_{13}$ – Mexico and $Cu_{11}NiSb_4S_{13}$ – Peru mineral corroborate the progressive improvement in the chemical homogeneity as the ball-milling increases, explaining why the two phases are no longer observable after 60 min of ball milling. Note that only Ni and As and Ni and Zn were observed for the mixtures with the Mexico and Peru minerals, respectively, since Ni is the only element absent in the chemical composition of these minerals. In the case of mixtures based on $Cu_{12}Sb_4S_{13}$, the ball-milling process does not lead to the disappearance of the small amount of the Cu_3SbS_4 phase (Figure 4) initially present in the PXRD pattern of the synthetic tetrahedrite. This analysis further reinforces the conclusion that ball-milling reduces the grain size of the two tetrahedrite phases without altering their respective chemical compositions.

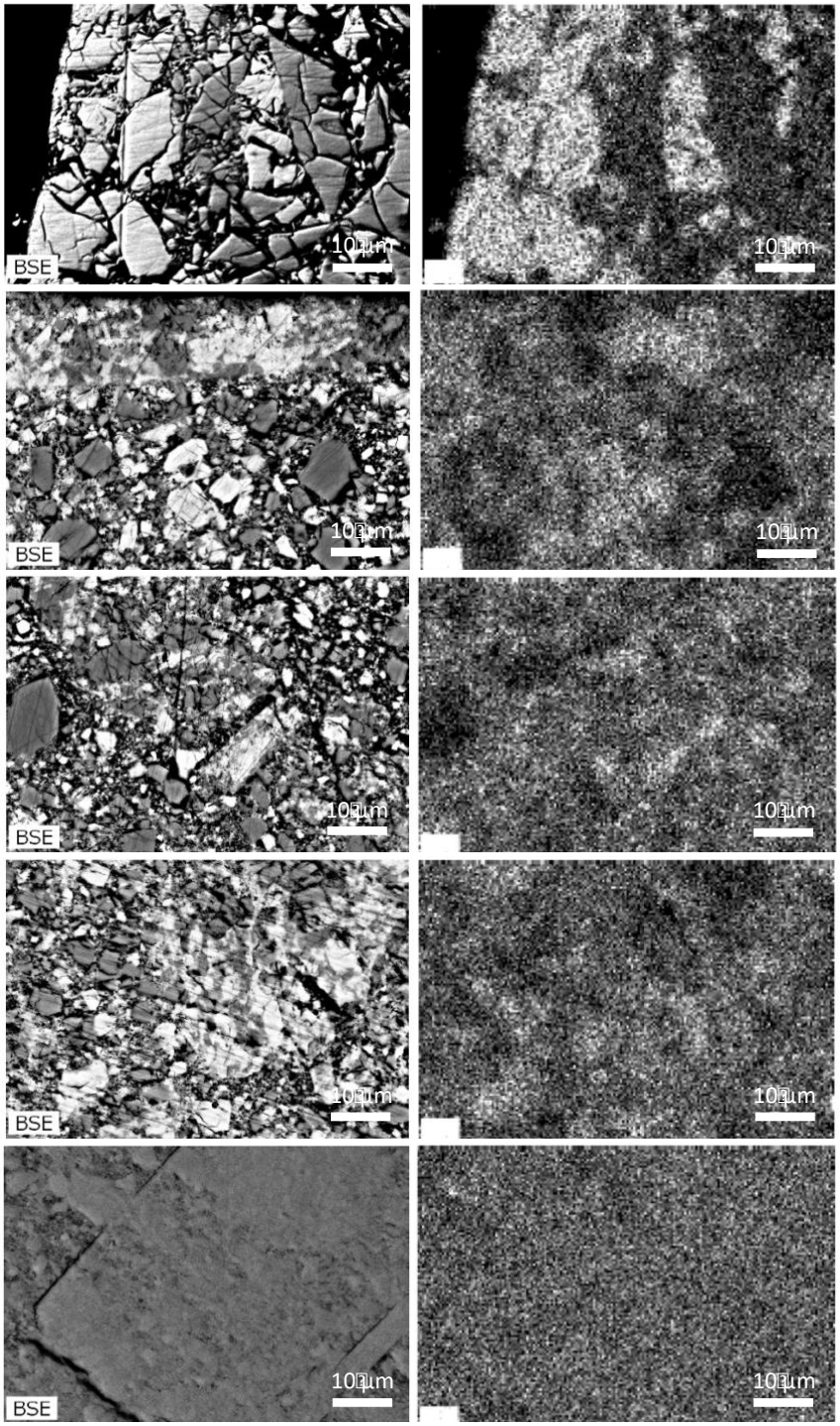

Figure 2. (Left panels) Backscattered electron images of the 50:50 mixture of synthetic ($Cu_{12}Sb_4S_{13}$) and natural tetrahedrites after (from top to bottom) 0, 10, 20, 30 and 60 minutes of ball milling. The darker color indicates the natural phase while the lighter color corresponds to the synthetic phase. (right panels) Evolution of the distribution of Sb in the synthetic-mineral

tetrahedrite mixture during ball milling, as determined by EDX spectroscopy. The areas shown are the same as those in the BSE images.

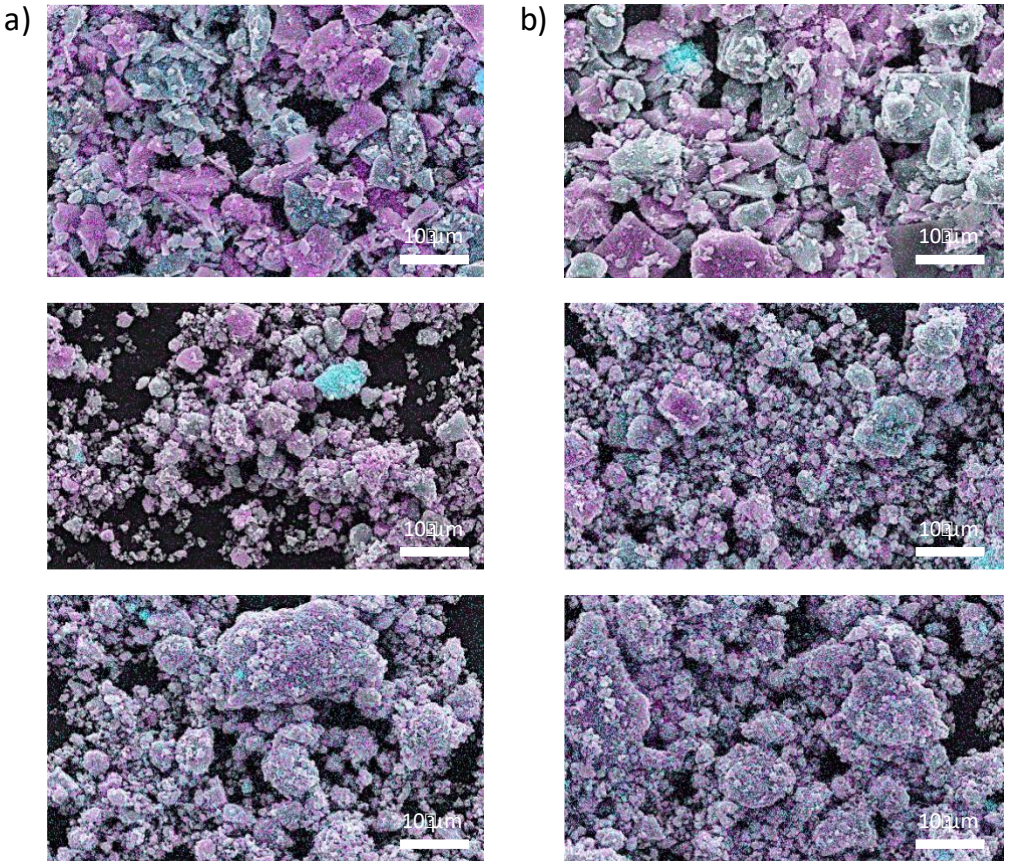

Figure 3. EDXS maps of 50:50 mixed powders of the synthetic $Cu_{11}NiSb_4S_{13}$ tetrahedrite with the a) Mexico mineral and b) Peru mineral after 0 (upper panels), 10 (middle panels) and 30 minutes (lower panels) of ball milling. In all panels, the light blue color corresponds to Ni while the pink color corresponds to either As (Mexico) or Zn (Peru).

The two-phase nature of the ball-milled powders is radically affected by spark plasma sintering at high temperatures. The evolution of the PXRD pattern can be better appreciated in Figure 4a and 4b, which shows a comparison of the patterns collected before and after sintering for the two illustrative mixtures $Cu_{12}Sb_4S_{13}$ – Peru and $Cu_{11}NiSb_4S_{13}$ – France.

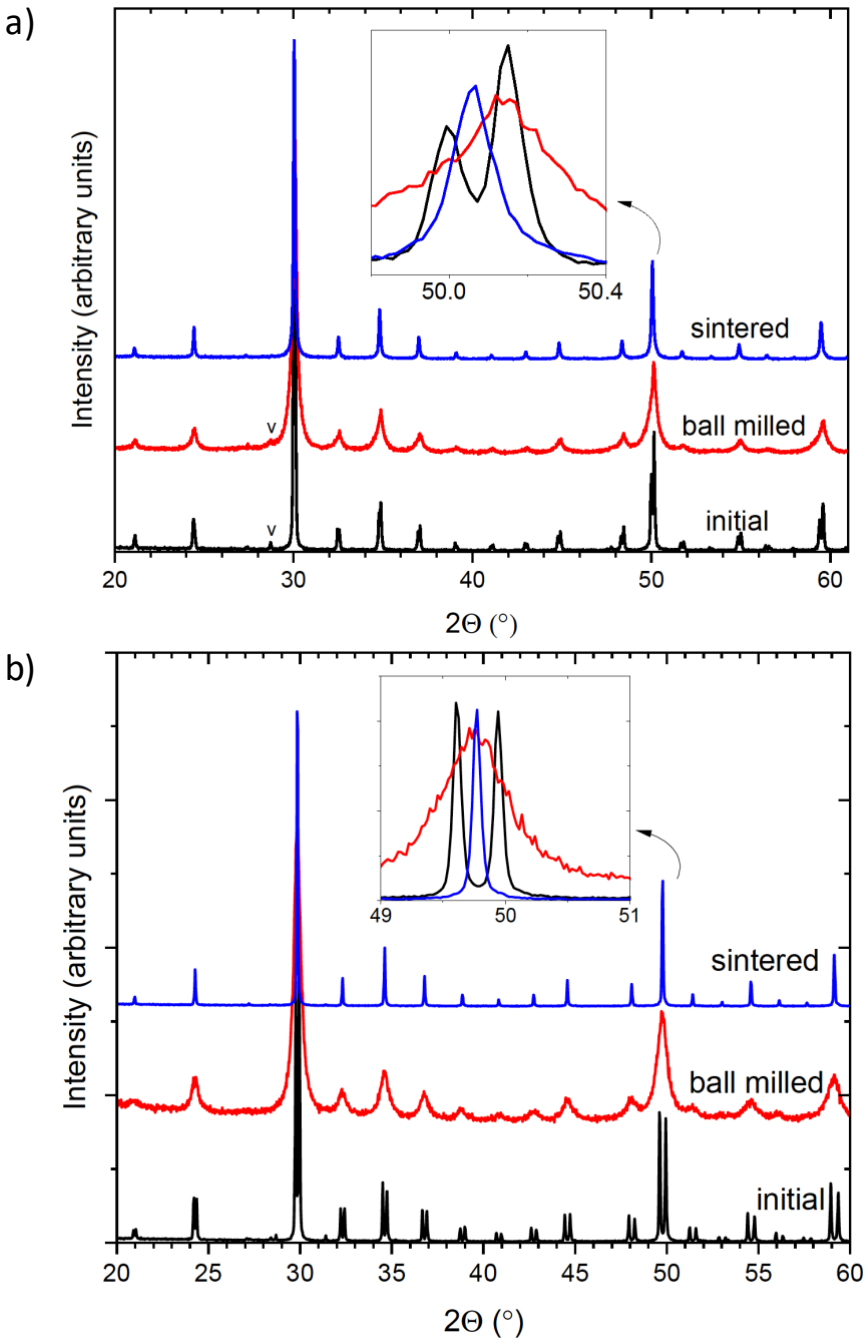

Figure 4. Comparison of the PXRD pattern of the initial (that is, non-milled), ball-milled and sintered mixture of a) synthetic $Cu_{12}Sb_4S_{13}$ and Peru mineral and b) synthetic $Cu_{11}NiSb_4S_{13}$ and France mineral. The minute amount of the Cu_3SbS_4 phase is marked by the "v" symbol.

The insets clearly show that a single diffraction peak results from the merging of the two peaks initially present, implying that a solid solution of the two phases has formed during the SPS

process. The lattice parameter of the new tetrahedrite phase corresponds to an average of those of the two phases (a = 10.300(2) Å for the $Cu_{12}Sb_4S_{13}$ – Peru mixture). SEM images collected on the consolidated samples confirm the formation of a single tetrahedrite phase for both series, which appear chemically homogeneous, at least down to the spatial resolution limit of this technique (≈1 μm). This remarkable merging of the two tetrahedrite phases after only few minutes of sintering is likely caused by the small grain size achieved after ball-milling, which favors the chemical reactivity during the SPS process. The fact that the grain size is the key parameter to obtain a homogenous, single-phased compound after SPS is corroborated by results obtained on the sample of the same initial composition that was only hand-ground prior to consolidation. As shown by both PXRD and SEM experiments (Figure S1 in the Supporting Information), the larger grain size prevented the formation of a solid solution on the time scale used for the consolidation step. The merging of the two tetrahedrite phases was equally observed for all the samples (Figure S2 in the Supporting Information), with the exception of the mixture of synthetic $Cu_{11}NiSb_4S_{13}$ and Mexico mineral. In this case, the final diffraction peaks do not correspond to an average of the two peaks observed prior to consolidation suggesting that the consolidation time was not sufficient to achieve a chemically-homogeneous sample.

This last result is in agreement with elemental X-ray maps performed on the final consolidated pellets (Figure 5 and Figures S3 and S4 in the Supporting Information). The $Cu_{11}NiSb_4S_{13}$ – Mexico mineral mixture still shows small Sb-rich and Ni-rich areas, indicating an incomplete diffusion of the elements between the grains during the SPS process (Figure S4 in the Supporting Information). For all other samples, the various elements are homogeneously distributed, with the notable exception of series with $Cu_{11}NiSb_4S_{13}$ for which small Ni-rich areas can be observed in the three final samples. The thermal stability of the tetrahedrite phase up to ~650 K evidenced in prior studies[31,36] on chemically-homogeneous samples should be

preserved in the present mixed samples. For this reason, the transport properties measurements presented hereafter were performed up to 623 K.

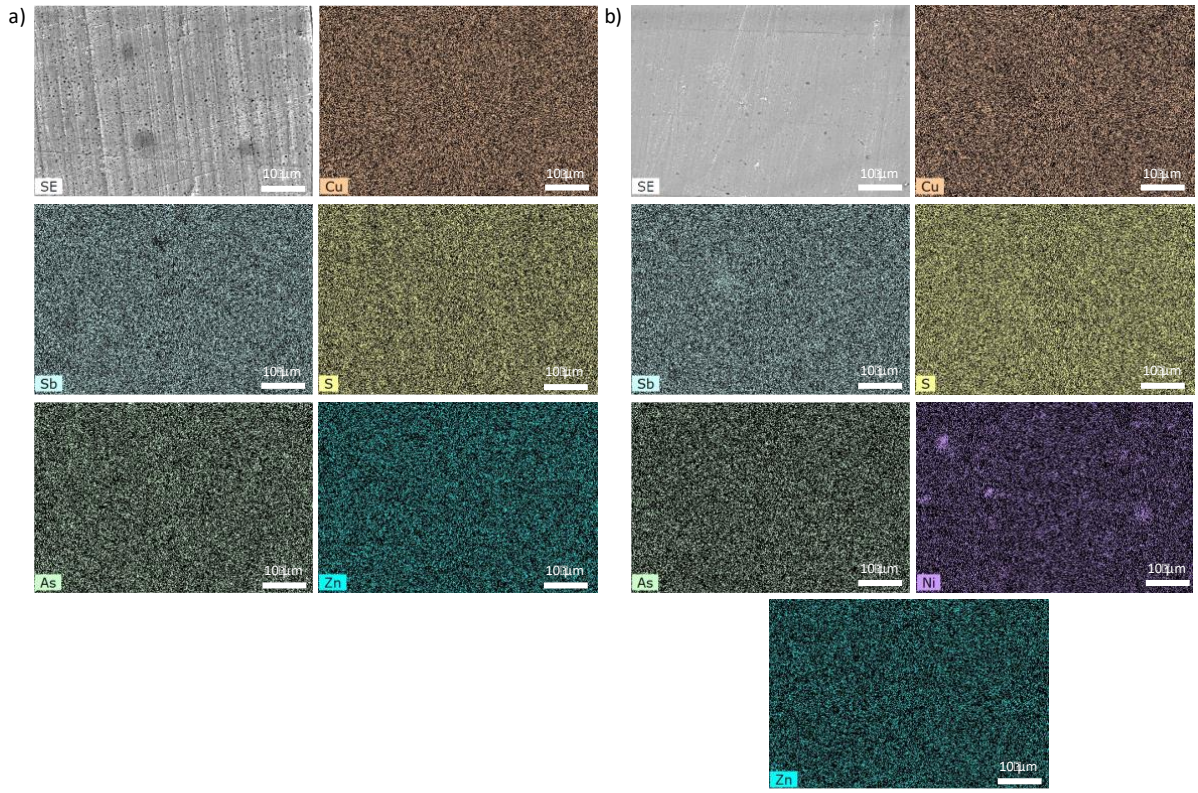

Figure 5. SEM images in backscattered electron mode along with the corresponding elemental X-ray maps of the final consolidated pellets of the a) synthetic $Cu_{12}Sb_4S_{13}$ and Peru mineral and b) synthetic $Cu_{11}NiSb_4S_{13}$ and Peru mineral. In both cases, the main elements are shown. Ag, present as traces in the mineral, has not been included in these analyses.

Transport properties

Figures 6a and 6b show the temperature dependence of the electrical resistivity ρ and thermopower α, respectively, of the different samples studied. The data collected on the pure synthetic samples have been added for comparison purposes. Except for the mixed natural-ternary sample, which shows a metallic-like character, all the samples retain the semiconducting-like behavior characteristic of the minerals down to 5 K (Figures S5 to S7 in

the Supporting Information).[28,56] However, mixing with the synthetic tetrahedrites strongly decreases the ρ values at 300 K by four orders of magnitude from values on the order of 0.1 Ω.m in the minerals (Figure S8) to values ranging between 10 and 600 μΩ.m. While the less conducting samples tend to show the highest α values, the France-Ni-tetrahedrite sample does not follow this simple trend with lower ρ values than the Mexico sample, despite the similar α values exhibited by both samples. This difference may be due to the differing composition of the minerals or to differences in the respective microstructure of these two samples.

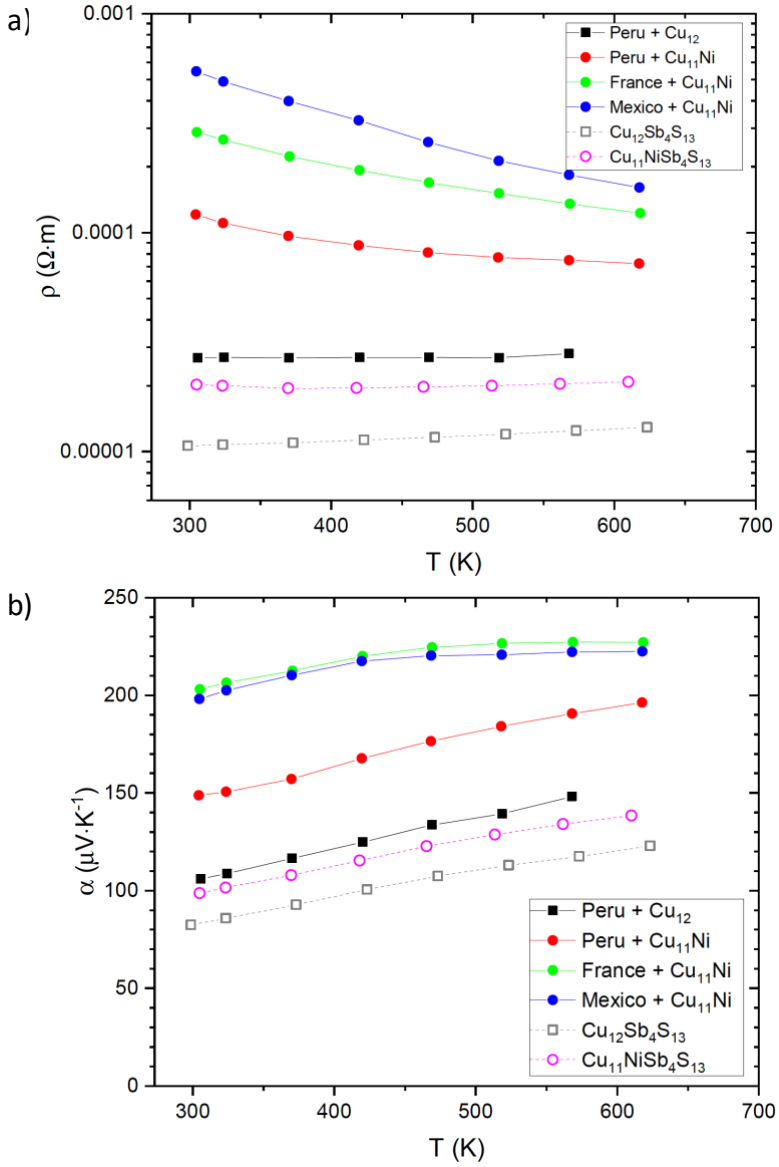

Figure 6. Temperature dependence of the electrical resistivity ρ (a) and thermopower α (b) of the various synthetic-natural tetrahedrite mixtures.

An important aspect of these results is that the resulting electronic properties of the final tetrahedrite are not a mere average of those of the synthetic and natural tetrahedrites but depend on their initial compositions. Interestingly, the Peru mineral mixed with the ternary tetrahedrite exhibits the lowest ρ and α values which only slightly differ from those of the pure synthetic $Cu_{12}Sb_4S_{13}$ and $Cu_{11}NiSb_4S_{13}$ samples. In contrast, all the other samples mixed with $Cu_{11}NiSb_4S_{13}$ show a more pronounced increase in ρ and α with respect to pure $Cu_{11}NiSb_4S_{13}$. These results tend to show that the initial chemical composition of the synthetic phase and hence, the degree of valence band filling, controls the final electronic properties of the mixed samples. The best compromise between high α and low ρ values seems to be achieved in samples mixed with the ternary $Cu_{12}Sb_4S_{13}$ which exhibits the most pronounced metallic character among known tetrahedrites. As shown in Figure 7, the highest power factor is obtained in this sample which is close to that measured for the pure synthetic tetrahedrite $Cu_{11}NiSb_4S_{13}$.

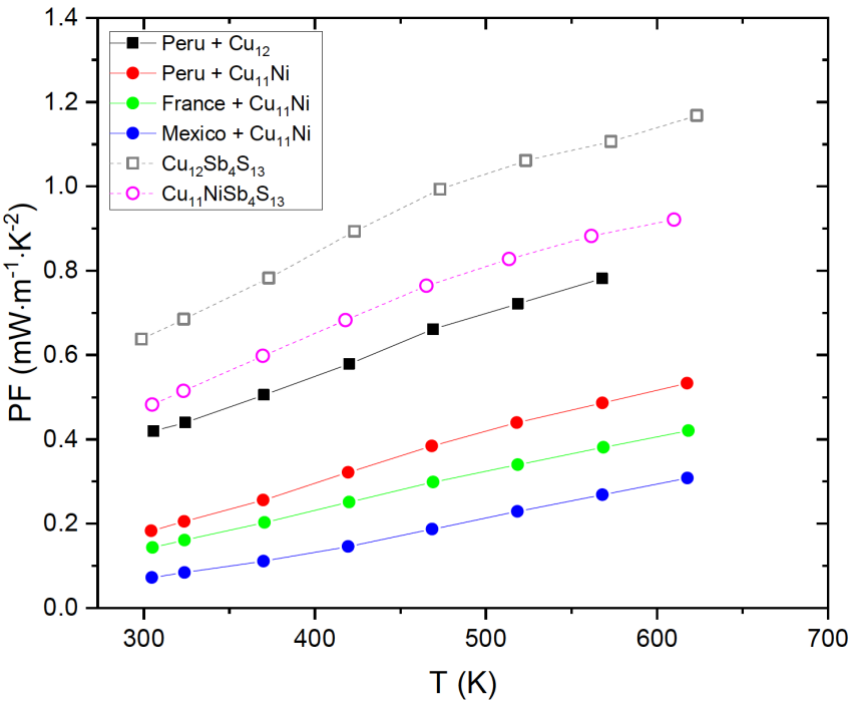

Figure 7. Power factor α^2/ρ as a function of temperature of the different synthetic-natural tetrahedrite mixtures studied.

The trend observed on $\rho(T)$ affects the evolution of the total thermal conductivity κ (Figure 8) through a decrease in the electronic thermal conductivity κ_e with increasing ρ according to the Wiedemann-Franz relation $\kappa_e = LT/\rho$, where L is the Lorenz number. The difference observed between the samples directly reflects the variations in κ_e. In the most insulating samples, the κ_e values are negligible so that the total and lattice thermal conductivities are nearly equal $\kappa \approx \kappa_L$. As commonly observed in tetrahedrites,[26-54] the κ_L values remain below 0.7 W m^{-1} K^{-1} in the whole temperature range and are weakly affected by the initial composition of the natural and synthetic tetrahedrites. The glass-like temperature dependence of all samples originates from the trigonally-coordinated Cu atoms that give rise to strongly-anharmonic, low-energy optical phonon modes, observed experimentally and reproduced by lattice dynamics calculations.[32,33,35,49,54]

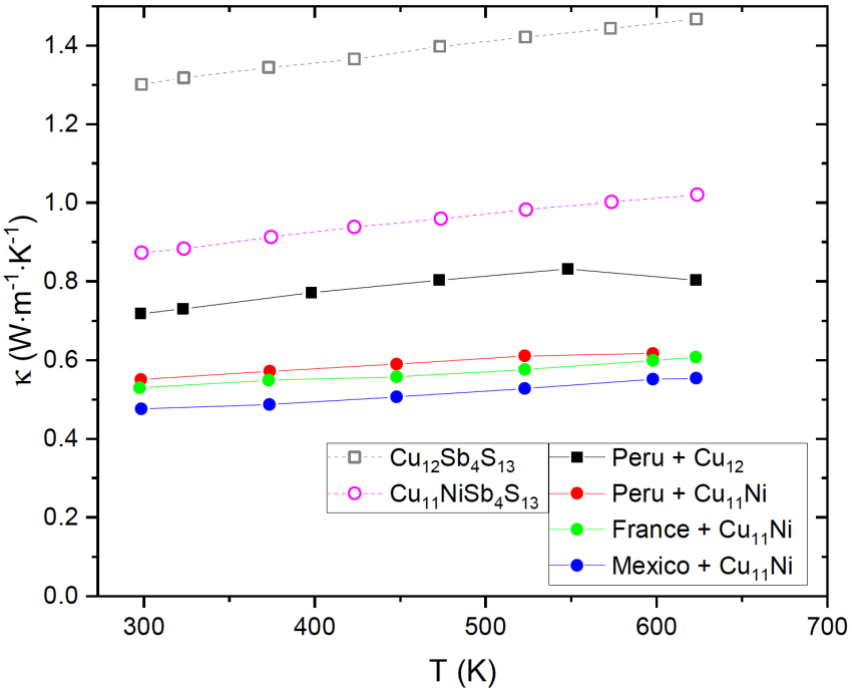

Figure 8. Temperature dependence of the total thermal conductivity κ of the different synthetic-natural tetrahedrite mixtures.

The thermoelectric performance of pure minerals is rather poor with a peak *ZT* value of 0.1 at 670 K, mainly due to high electrical resistivity (Figure S8). In contrast, mixing synthetic tetrahedrites with minerals yields enhanced dimensionless thermoelectric figure of merit *ZT* ranging between 0.4 and 0.6 at 623 K (Figure 9). Remarkably, the *ZT* values of the Peru+$Cu_{12}Sb_4S_{13}$ sample are higher than those measured in synthetic $Cu_{12}Sb_4S_{13}$. These results demonstrate that mixing synthetic and natural tetrahedrites in a 50:50 ratio can improve the thermoelectric performance at high temperatures with respect to the pure synthetic compound.

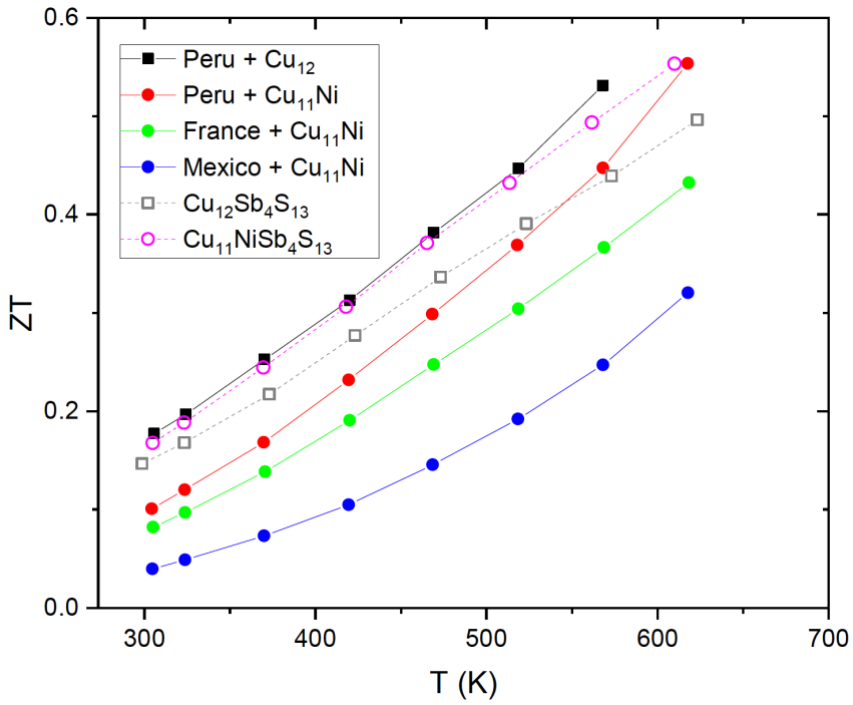

Figure 9. Dimensionless thermoelectric figure of merit *ZT* as a function of temperature of the various synthetic-natural tetrahedrite mixtures.

Conclusions

We reported on the synthesis and high-temperature thermoelectric properties of tetrahedrites prepared from an equal ratio of synthetic ($Cu_{12}Sb_4S_{13}$ or $Cu_{11}NiSb_4S_{13}$) and natural tetrahedrites coming from Europe and the Americas. These initially synthetic-natural composites were

subjected to a combination of ball-milling followed by spark plasma sintering. PXRD and SEM analyses reveal that ball-milling only decreases the crystallite size without any evident reactions between the two tetrahedrite phases. Remarkably, the significantly lower grain size is likely the key parameter which facilitates a solid-state diffusion reaction during speak plasma sintering which yields a dense, chemically-homogeneous tetrahedrite phase within only few minutes. Measurements of the thermoelectric properties demonstrate that the resulting tetrahedrite phase exhibits thermoelectric performances similar to those achieved in pure synthetic compounds. Mixing with either $Cu_{12}Sb_4S_{13}$ or $Cu_{11}NiSb_4S_{13}$ is, however, not strictly equivalent, likely due to the different valence electron count of both compounds which governs the hole concentration of the final compound. The results show that the metallic character of the synthetic phase is an important parameter to achieve near optimum doping and hence, maintain high thermoelectric performance at high temperatures. Peak *ZT* values ranging between 0.4 and 0.6 at 623 K have been achieved in the different samples studied demonstrating that mixing synthetic tetrahedrites with minerals is a viable strategy to produce bulk dense tetrahedrite samples with optimized thermoelectric properties. Further investigations would be nevertheless worthwhile to pursue in order to determine the influence of the SPS parameters on the thermoelectric properties of the final sample. The completeness of the diffusion-driven merging of the two initial tetrahedrite phases may be an important aspect to achieve a better control of the electronic properties. Finally, the fact that higher *ZT* values have been reported in a prior study indicates that further enhancement may be achieved by variations in the chemical composition of the mineral or by varying the initial ratio slightly away from the 50:50 ratio used herein.

Experimental Methods

Synthesis: All the manipulations of the starting elements, powders and loadings of the ball-milling jars were realized in a dry, argon-filled glovebox.

Synthetic tetrahedrites with the compositions $Cu_{12}Sb_4S_{13}$ and $Cu_{11}NiSb_4S_{13}$ were prepared by direct reactions of stoichiometric amounts of Cu (99.99%, ChemPur), Ni (99.99%, Alfa Aesar), Sb (99.999%, 5N+) and S (99.999%, Strem Chemicals) powders in silica tubes sealed under secondary vacuum. The tubes were placed in a rocking furnace and slowly heated up to 923 K with a heating rate of 0.3 K min^{-1} to avoid an excessive internal pressure due to the high vapor pressure of sulfur. After maintaining the tubes at this temperature for 12h, they were cooled down to room temperature with a cooling rate of 0.5 K min^{-1}. The obtained ingots were then hand-ground in an agate mortar, cold-pressed into pellets, and again sealed in evacuated silica tubes. The tubes were annealed at 723 K for 5 days and quenched in cold water. The annealed pellets were hand-crushed in an agate mortar and the crystal structure and phase purity were verified by laboratory powder X-ray diffraction (PXRD) measurements. While the Ni-containing tetrahedrite was found to be single phase based on its PXRD pattern, a small amount of the Cu_3SbS_4 phase was detected in the ternary tetrahedrite.

The powders of synthetic and natural tetrahedrites were mixed using a planetary ball milling system (Fritsch Pulverisette 7 premium line). The tetrahedrite minerals used herein originate from mines in Peru, Mexico and France (Isère). Bulk pieces were reduced in powders by hand-grinding in an agate mortar. During this step, care was taken to remove evident pieces of quartz present as inclusions in the minerals as well as occasional chalcopyrite layers on the surface. The powders, with a synthetic-to-natural mass ratio of 50:50, were loaded into a 20 ml ZrO_2 jar containing ZrO_2 balls of 10 mm in diameter. In all cases, the total mass of powders was 3g with which six balls were placed to reach a 6:1 ball-to-powder ratio. The powders were

then processed for 90 min at a speed of 900 rotations per minute. This process was realized under inert atmosphere which was ensured by the presence of a lid and a silicone O-ring on the jars constituting an overall airproof assembly. A small amount of powders was harvested from the jars at regular time intervals which were subsequently analyzed by powder X-ray diffraction. For comparison purposes, one sample was prepared by mixing powders of synthetic and natural tetrahedrites in a 50:50 ratio, hand-ground in an agate mortar, that is, not subjected to any ball milling.

After ball-milling or hand-grinding, the mixed powders were consolidated in a graphite die (10 mm in diameter) by spark plasma sintering at 723 K under an uniaxial pressure of 80 MPa for 4 minutes. The density, determined from the weight and geometrical dimensions, was found to be above 95% of the theoretical density for all samples.

Structural and chemical characterizations: Powder X-ray diffraction measurements were carried out at 300 K using a D8 Advanced diffractometer (Bruker) using the $CuK\alpha_1$ radiation. The lattice parameters *a* of the cubic unit cell were inferred by Rietveld refinements against the PXRD data using the Fullprof software.[58]

The chemical homogeneity and spatial distribution of the elements were determined by scanning electron microscopy (SEM) using a Quanta FEG 650 instrument (FEI) equipped with a Bruker Quantax detector for energy dispersive X-ray spectroscopy (EDXS). For these analyses, bulk pieces of the samples were carefully polished with sand paper down to 4000 grit.

Quantitative chemical analyses were performed by electron probe microanalyses (EPMA) on mirror-polished, carbon-coated dense bulk pieces using a Cameca SX 100 microprobe. The concentrations of Cu, Ag, Zn, Fe, Co, Sb, As and S in the three minerals were determined by using $CuFeS_2$, Ag, ZnS, FeS_2, Co, Sb_2S_3, GaAs and $CuFeS_2$, respectively, as standards. No other elements were detected using EDXS. The chemical compositions, listed in Table 1, were

obtained by averaging about 30 different measurement spots and by normalizing the chemical compositions to 29 atoms per formula unit.

Transport properties measurements: Prior to measurements, the consolidated cylindrical pellets were cut into bars and cylinders of appropriate geometrical dimensions for transport property measurements using a diamond-wire saw.

Electrical resistivity, thermopower and thermal conductivity were measured simultaneously between 5 and 300 K using a home-made instrument employing the four-probe method. Four silver wires (0.2 mm in diameter) were attached to bar-shaped samples of typical dimensions 2×2×8 mm^3 with a minute amount of conductive nickel paint. We note that due to the very high ρ values reached at 5 K in all samples, $\alpha(T)$ could be only followed down to 10 – 30 K depending on the composition of the sample. Hence, the data measured below this temperature have been discarded.

Electrical resistivity and thermopower were simultaneously measured on bars of typical dimensions 2×2×8 mm^3 between 300 and 623 K using a ZEM-3 apparatus (Ulvac-Riko) under a low He pressure. Thermal conductivity was determined in the temperature range 300 – 623 K via thermal diffusivity measurements on cylindrical samples (10 mm in diameter, 1 mm in thickness) using a LFA 427 instrument (Netzsch). The samples were graphite-coated prior to measurements. The thermal conductivity was calculated by the relation $\kappa = \rho_V d C_p$ where ρ_V is the density, d is the thermal diffusivity and C_p is the isobaric specific heat. The temperature dependence of ρ_V has been neglected. C_p has been calculated using the Dulong-Petit law and hence, has been considered as temperature-independent as a first approximation. The experimental uncertainties in κ, α and ρ are estimated to be 10, 5 and 5%, respectively. The combined experimental uncertainty on the *ZT* values between 300 and 700 K is estimated to be ~17%.[59]

Acknowledgements

The authors acknowledge the financial support from the French National Agency (ANR) in the frame of the project MASSCOTE ("Matériaux sulfures à structures complexes: application à la thermoélectricité", project identifier ANR-15-CE05-0027). This work was performed with the financial support of the Operational Program Research, Development and Education (Center of Advanced Applied Sciences Project No. CZ.02.1.01/0.0/0.0/16_019/0000778). P. L. acknowledges the financial support of the French Ministry of Foreign Affairs.

Keywords: Ball-milling • Minerals • Tetrahedrites • Thermoelectric • Transport properties

Conflict of Interest

The authors declare no conflicts of interest.

Data Availability Statement

The data that support the findings of this study are available in this paper.

References

[1] D. M. Rowe, *Thermoelectrics and its Energy Harvesting*, CRC Press, Boca Raton, FL, **2012**.

[2] H. J. Goldsmid, *Thermoelectric Refrigeration*. Springer, New York, USA, **1964**.

[3] G. Tan, L.-D. Zhao, M. G. Kanatzidis, *Chem. Rev.* **2016**, *116*, 12123–12149.

[4] X.-L. Shi, J. Zou, Z.-G. Chen, *Chem. Rev.* **2020**, *120*, 7399–7515.

[5] Y. He, T. Day, T. Zhang, H. Liu, X. Shi, L. Chen, G. J. Snyder, *Adv. Mater.* **2014**, *26*, 3974–3978.

[6] G. Dennler, R. Chmielowski, S. Jacob, F. Capet, P. Roussel, S. Zastrow, K. Nielsch, I. Opahle, G. K. H. Madsen, *Adv. Energy Mater.* **2014**, *4*, 1301581.

[7] P. Qiu, T. Zhang, Y. Qiu, X. Shi, L. Chen, *Energy Environ. Sci.* **2014**, *7*, 4000–4006.

[8] S. O. J. Long, A. V. Powell, P. Vaqueiro, S. Hull, *Chem. Mater.* **2018**, *30*, 456–464.

[9] H. Xie, X. Su, T. P. Bailey, C. Zhang, W. Liu, C. Uher, X. Tang, M. G. Kanatzidis, *Chem. Mater.* **2020**, *32*, 2639–2646.

[10] R. Ang, A. U. Khan, N. Tsujii, K. Takai, R. Nakamura, T. Mori, *Angew. Chem. Int. Ed.* **2015**, *54*, 12909–12913.

[11] Y. Li, T. Zhang, Y. Qin, T. Day, G. J. Snyder, X. Shi, L. Chen, *J. Appl. Phys.* **2014**, *116*, 203705.

[12] E. Isotta, B. Mukherjee, C. Fanciulli, N. M. Pugno, P. Scardi, *J. Phys. Chem. C* **2020**, *124*, 7091–7096.

[13] D. Zhang, J. Yang, Q. Jiang, Z. Zhou, X. Li, J. Xin, A. Basit, Y. Ren, X. He, *Nano Energy* **2017**, *36*, 156–165.

[14] K. Suekuni, T. Takabatake, *APL Mater.* **2016**, *4*, 104503.

[15] K. Suekuni, F. S. Kim, H. Nishiate, M. Ohta, H. I. Tanaka, T. Takabatake, *Appl. Phys. Lett.* **2014**, *105*, 132107.

[16] C. Bourgès, Y. Bouyrie, A. Supka, R. Al Rahal Al Orabi, P. Lemoine, O. Lebedev, M. Ohta, K. Suekuni, V. Nassif, V. Hardy, R. Daou, Y. Miyazaki, M. Fornari, E. Guilmeau, *J. Am. Chem. Soc.* **2018**, *140*, 2186–2195.

[17] V. Pavan Kumar, A. R. Supka, P. Lemoine, O. I. Lebedev, B. Raveau, K. Suekuni, V. Nassif, R. Al Rahal Al Orabi, M. Fornari, E. Guilmeau, *Adv. Energy Mater.* **2019**, *9*, 1–11.

[18] Y. Bouyrie, M. Ohta, K. Suekuni, Y. Kikuchi, P. Jood, A. Yamamoto, T. Takabatake, *J. Mater. Chem. C* **2017**, *5*, 4174–4184.

[19] T. Deng, P. Qiu, Q. Song, H. Chen, T.-R. Wei, L. Xi, X. Shi, L. Chen, *J. Appl. Phys.* **2019**, *126*, 085111.

[20] Y. Shen, C. Li, R. Huang, R. Tian, Y. Ye, L. Pan, K. Koumoto, R. Zhang, C. Wan, Y. Wang, *Sci. Rep.* **2016**, *6*, 32501.

[21] H. Zhao, X. Xu, C. Li, R. Tian, R. Zhang, R. Huang, Y. Lyu, D. Li, X. Hu, L. Pan, Y. Wang, *J. Mater. Chem. A* **2017**, *5*, 23267–23275.

[22] Q. Tan, W. Sun, Z. Li, J.-F. Li, *J. Alloys Compd.* **2016**, *672*, 558–563.

[23] V. Pavan Kumar, P. Lemoine, V. Carnevali, G. Guélou, O. I. Lebedev, P. Boullay, B. Raveau, R. Al Rahal Al Orabi, M. Fornari, C. Prestipino, D. Menut, C. Candolfi, B. Malaman, J. Juraszek, E. Guilmeau, *J. Mater. Chem. A* **2021**, *9*, 10812–10826.

[24] V. Pavan Kumar, P. Lemoine, V. Carnevali, G. Guélou, O. I. Lebedev, B. Raveau, R. Al Rahal Al Orabi, M. Fornari, C. Candolfi, C. Prestipino, D. Menut, B. Malaman, J. Juraszek, K. Suekuni, E. Guilmeau, *Inorg. Chem.* **2021**, *60*, 16273–16285.

[25] G. Guélou, V. Pavan Kumar, V. Carnevali, O. I. Lebedev, B. Raveau, C. Couder, C. Prestipino, P. Lemoine, B. Malaman, J. Juraszek, C. Candolfi, B. Lenoir, R. Al Rahal Al Orabi, M. Fornari, E. Guilmeau, *Chem. Mater.* **2021**, *33*, 9425–9438.

[26] K. Suekuni, K. Tsuruta, T. Ariga, M. Koyano, *Appl. Phys. Express* **2012**, *5*, 051201.

[27] X. Lu, D. T. Morelli, Y. Xia, F. Zhou, V. Ozolins, H. Chi, X. Zhou, C. Uher, *Adv. Energy Mater.* **2013**, *3*, 342-348.

[28] X. Lu, D. T. Morelli, *Phys. Chem. Chem. Phys.* **2013**, *15*, 5762–5766.

[29] K. Suekuni, K. Tsuruta, M. Kunii, H. Nishiate, E. Nishibori, S. Maki, M. Ohta, A. Yamamoto, M. Koyano, *J. Appl. Phys.* **2013**, *113*, 043712.

[30] R. Chetty, D. S. Prem Kumar, G. Rogl, P. Rogl, E. Bauer, H. Michor, S. Suwas, S. Puchegger, G. Giester, R. C. Mallik, *Phys. Chem. Chem. Phys.* **2015**, *17*, 1716–1727.

[31] T. Barbier, P. Lemoine, S. Gascoin, O. I. Lebedev, A. Kaltzoglou, P. Vaqueiro, A. V. Powell, R.I. Smith, E. Guilmeau, *J. Alloys Compd.* **2015**, *634*, 253–262.

[32] Y. Bouyrie, C. Candolfi, S. Pailhès, M. M. Koza, B. Malaman, A. Dauscher, J. Tobola, O. Boisron, L. Saviot, B. Lenoir, *Phys. Chem. Chem. Phys.* **2015**, *17*, 19751–19758.

[33] E. Lara-Curzio, A. F. May, O. Delaire, M. A. McGuire, X. Lu, C.-Y. Liu, E. D. Case, D. T. Morelli, *J. Appl. Phys.* **2014**, *115*, 193515.

[34] R. Chetty, A. Bali, M. H. Naik, G. Rogl, P. Rogl, M. Jain, S. Suwas, R. C. Mallik, *Acta Mater.* **2015**, *100*, 266–274.

[35] W. Lai, Y. Wang, D. T. Morelli, X. Lu, *Adv. Funct. Mater.* **2015**, *25*, 3648–3657.

[36] Y. Bouyrie, C. Candolfi, V. Ohorodniichuk, B. Malaman, A. Dauscher, J. Tobola, B. Lenoir, *J. Mater. Chem. C* **2015**, *3*, 10476–10487.

[37] X. Lu, D. T. Morelli, *J. Electron. Mater.* **2014**, *43*, 1983–1987.

[38] X. Lu, D. T. Morelli, Y. Xia, V. Ozolins, *Chem. Mater.* **2015**, *27*, 408–413.

[39] Y. Bouyrie, C. Candolfi, J.-B. Vaney, A. Dauscher, B. Lenoir, *J. Electron. Mater.* **2016**, *45*, 1601–1605.

[40] Y. Bouyrie, C. Candolfi, A. Dauscher, B. Malaman, B. Lenoir, *Chem. Mater.* **2015**, *27*, 8354–8361.

[41] Y. Bouyrie, S. Sassi, C. Candolfi, J-B. Vaney, A. Dauscher, B. Lenoir, *Dalton Trans.* **2016**, *45*, 7294–7302.

[42] X. Lu, D. T. Morelli, Y. Wang, W. Lai, Y. Xia, V. Ozolins, *Chem. Mater.* **2016**, *28*, 1781–1786.

[43] Y. Kosaka, K. Suekuni, K. Hashikuni, Y. Bouyrie, M. Ohta, T. Takabatake, *Phys. Chem. Chem. Phys.* **2017**, *19*, 8874–8879.

[44] D. S. Prem Kumar, R. Chetty, P. Rogl, G. Rogl, E. Bauer, P. Malar, R. C. Mallik, *Intermetallics* **2016**, *78*, 21–29.

[45] P. Vaqueiro, G. Guélou, A. Kaltzoglou, R. I. Smith, T. Barbier, E. Guilmeau, A.V. Powell,

Chem. Mater. **2017**, *29*, 4080–4090.

[46] P. Levinský, C. Candolfi, A. Dauscher, B. Lenoir, J. Hejtmánek, *J. Electron. Mater.* **2019**, *48*, 1926–1931.

[47] N. Ghassemi, Y. Tian, X. Lu, Y. Yan, X. Zhou, J. H. Ross Jr, *J. Phys. Chem. C* **2021**, *125*, 18877–18886.

[48] S. O. Long, A. V. Powell, S. Hull, F. Orlandi, C. C. Tang, A. R. Supka, M. Fornari, P. Vaqueiro, *Adv. Funct. Mater.* **2020**, *30*, 1909409.

[49] Y. Xia, V. Ozolins, C. Wolverton, *Phys. Rev. Lett.* **2020**, *125*, 085901.

[50] K. Umeo, K. Suekuni, T. Takabatake, E. Nishibori, *Phys. Rev. B* **2020**, *102*, 100302.

[51] T. Barbier, S. Rollin-Martinet, P. Lemoine, F. Gascoin, A. Kaltzoglou, P. Vaqueiro, A. V. Powell, E. Guilmeau, *J. Am. Ceram. Soc.* **2015**, *99*, 51–56.

[52] D. J. James, X. Lu, D. T. Morelli, S. L. Brock, *ACS Appl. Mater. Interfaces* **2015**, *7*, 23623–23632.

[53] A. P. Gonçalves, E. B. Lopes, J. Monnier, J. Bourgon, J.-B. Vaney, A. Piarristeguy, A. Pradel, B. Lenoir, G. Delaizir, M. F. C. Pereira, E. Alleno, C. Godart, *J. Alloys Compd.* **2016**, *664*, 209–217.

[54] A. F. May, O. Delaire, J. L. Niedziela, E. Lara-Curzio, M. A. Susner, D. L. Abernathy, M. Kirkham, M. A. McGuire, *Phys. Rev. B* **2016**, *93*, 064104.

[55] F. Neves, L. Esperto, I. Figueira, J. Mascarenhas, R. Salgueiro, T. P. Silva, J. B. Correia, P. A. Carvalho, D. de Oliveira, *Miner. Eng.* **2021**, *164*, 106833.

[56] P. Levinský, J.-B. Vaney, C. Candolfi, A. Dauscher, B. Lenoir, J. Hejtmánek, *J. Electron. Mater.* **2016**, *45*, 1351–1357.

[57] X. Fan, E. D. Case, X. Lu, D. T. Morelli, *J. Mater. Sci.* **2013**, *48*, 7540–7550.

[58] J. Rodriguez-Carvajal, *Physica B* **1993**, *192*, 55–69.

[59] E. Alleno, D. Bérardan, C. Byl, C. Candolfi, R. Daou, R. Decourt, E. Guilmeau, S. Hébert, J. Hejtmanek, B. Lenoir, P. Masschelein, V. Ohorodniichuk, M. Pollet, S. Populoh, D. Ravot, O. Rouleau, M. Soulier, *Rev. Sci. Instrum.* **2015**, *86*, 011301.

Entry for the Table of Contents

Maintaining the high thermoelectric performance of synthetic tetrahedrites in composites obtained by mixing them with mineral ore in a 50-50 ratio is demonstrated. This simple process may be beneficial to reach cost-efficiency in large-scale production of thermoelectric sulfides.